Journal of Materials Chemistry A

ROYAL SOCIETY OF CHEMISTRY

PAPER

View Article Online
View Journal

Cite this: DOI: 10.1039/d6ta00904b

Imparting dispersibility and electrochemical activity to chlorine-terminated MXenes *via* oxygen enrichment

Kevinilo P. Marquez, [ab] Xinnian Li, [a] Rufus Mart Ceasar R. Ramos, [ac] Mia Judicpa, [ac] Behnam Akhavan, [de] Elmer S. Austria, Jr., [d] Si Qin, [a] Peter C. Sherrell, [f] Luke C. Henderson, [a] Jizhen Zhang, [ag] Ken Aldren S. Usman *[ai] and Joselito M. Razal *[ah]

Chlorine-terminated Ti_3C_2 MXenes (Cl-MXenes) demonstrate remarkable resistance to water- and oxygen-induced degradation, yet their hydrophobic nature limits compatibility with polar solvents. This is a stark contrast to the hydrophilic, oxygen-terminated MXenes produced through conventional fluoride-based etching. Capitalizing on the labile character of surface chlorine atoms, we developed a solution-based approach to create oxygen-enriched Cl-MXenes (O,Cl-MXenes) through delamination in alkaline dimethyl sulfoxide. This controlled functionalization yields mixed chlorine-oxygen terminations (a ~95% increase in the Ti–O/Ti–Cl ratio), substantially improving MXene dispersibility in organic solvents. Oxygen enrichment through direct addition at the Ti surface and partial chlorine substitution not only enhances dispersion stability and oxidation resistance (up to ~10 days) but also combines the anodic stability (+~0.2 V) of chlorine terminations with the high capacitive activity of oxygen groups. These results establish that co-functionalization with chlorine and oxygen produces MXenes with enhanced solution processability and environmental stability, offering a versatile materials design strategy for advancing MXene-based technologies.

Received 30th January 2026
Accepted 20th May 2026

DOI: 10.1039/d6ta00904b

rsc.li/materials-a

Introduction

MXenes, a family of two-dimensional transition metal nitrides and/or carbides, exhibit exceptional properties, including high conductivity,[1–3] strong electromagnetic interference shielding,[4,5] and excellent electrochemical performance.[6–8] Their solution processability further enables fabrication into diverse architectures.[9–12] The most extensively studied member, $Ti_3C_2T_x$, is typically produced by selectively etching aluminum from the Ti_3AlC_2 MAX phase. Common top–down etching methods include wet chemical approaches using fluoride-based[2,13] or fluoride-free solutions,[14,15] as well as high-temperature Lewis acid molten salt (LAMS) techniques.[16–19] While bottom–up methods such as chemical vapor deposition[20] offer precise, atomistic control over surface composition and facilitate the scalable production of chlorine-terminated MXenes (Cl-MXenes), they face challenges in delamination and processing, limiting their current practicality.

Wet-chemical etching remains the most common method for synthesizing MXene due to its operational simplicity and ability to produce highly conductive materials. This process yields MXene surfaces rich in proton-active oxygen terminations, which we have previously shown can be tuned to control interactions with solvents and electrolytes.[21] However, these MXenes are highly susceptible to oxidative degradation in aqueous environments,[22] and the etching process itself often involves hazardous reagents.

In contrast, the LAMS method employs safer, non-reactive salts while maintaining scalability. It produces MXenes terminated with halogens such as chlorine or iodine (Cl- or I-MXenes),[18,23] resulting in hydrophobic surfaces with superior oxidation resistance. A key advantage of these halogen-

[a]Institute for Frontier Materials, Deakin University, Geelong, VIC 3216, Australia. E-mail: k.usman@deakin.edu.au

[b]Institute of Chemistry, University of the Philippines, Los Baños, Laguna 4031, Philippines

[c]Manufacturing, Commonwealth Scientific and Industrial Research Organization (CSIRO), Waurn Ponds, VIC 3216, Australia

[d]School of Biomedical Engineering, The University of Sydney, Sydney, NSW 2006, Australia

[e]School of Engineering, College of Engineering, Science and Environment, University of Newcastle, Callaghan, NSW 2308, Australia

[f]Applied Chemistry & Environmental Science, STEM College, RMIT University, Melbourne, Victoria 3001, Australia

[g]Research Center for Materials Nanoarchitectonics, National Institute for Materials Science, 24 Namiki 1-1, Tsukuba 305-0044, Japan

[h]Joint Research Centre for Fiber Innovations and Renewable Materials, School of Fashion and Textiles, The Hong Kong Polytechnic University, Hong Kong SAR, 999077, China. E-mail: joselito.razal@polyu.edu.hk

[i]Institute of Chemistry, University of the Philippines, Diliman, Quezon City, 1101, Philippines. E-mail: ken_aldren.usman@upd.edu.ph

terminated surfaces is the lability of the Ti–Cl bonds towards many ligand substitution reactions including oxygen, nitrogen and chalcogens (Se, Te),[24,25] which allows for straightforward post-synthesis functionalization with various organic functional groups.[26] This tunability provides a versatile pathway to tailor MXene properties for specific applications, although the inherent hydrophobicity initially complicates delamination in polar solvents.[17] While bottom–up approaches such as chemical vapor deposition[20,27,28] offer precise, atomistic control over surface terminations and enable industrial-scale production of Cl-MXenes, the sophisticated infrastructure required remains inaccessible to many laboratories. Regardless, Cl-terminated MXenes produced through these methods are typically multilayered and continue to exhibit delamination and processing challenges, limiting their current practical utility.

In this study, we showed how the combined influence of surface chlorine and oxygen groups can be leveraged to enhance solvent dispersibility, electrochemical performance, and oxidation stability by synthesizing an oxygen-enriched, chlorine-terminated MXene (O,Cl-MXene) through delamination of multilayered Cl-MXene (prepared *via* the LAMS method) *via* lithium hydroxide (LiOH) in dimethyl sulfoxide (DMSO). For comparison, single-layer Cl-MXene was delaminated using lithium chloride (LiCl) in DMSO. We then systematically evaluated the behavior of both materials in various organic solvents and electrolyte systems.

The O,Cl-MXene exhibited superior colloidal stability across a broader range of solvents after four days, along with generally higher zeta potential values that in some cases matched those of conventional, *in situ* fluoride-etched MXenes (MILD-MXenes). This enhanced stability stems from the partial replacement of chlorine with oxygen-containing groups, which increases the material's affinity for polar solvents. Furthermore, O,Cl-MXene demonstrated better resistance to aqueous degradation over a 10 day period compared to MILD-MXene, a property we attribute to the persistence of protective, water-resistant chlorine surface groups.

We further demonstrate that mixed oxygen-chlorine terminations enhance electrochemical behavior. Cyclic voltammetry revealed that O,Cl-MXenes exhibits capacitances an order of magnitude greater across all electrolytes than those of Cl-MXenes, as well as a wider operational potential window than MILD-MXenes. Electrochemical impedance spectroscopy also showed consistently faster ion kinetics for O,Cl-MXene, demonstrating that oxygen enrichment successfully merges the environmental stability of chlorine terminations with the high electrochemical activity of oxygen functional groups. Overall, we show that this co-functionalization strategy provides a versatile pathway to engineer MXenes with the enhanced processability and stability required for practical applications. Overall, this co-functionalization strategy not only enhances MXene stability and processability but also provides a step towards precise control over surface terminations, thereby expanding the range of viable solution-processing routes and broadening the design space for MXene-based electrochemical and structural applications.

Results and discussion

Synthesis of Cl-MXene and O,Cl-MXene

Chlorine-terminated Ti_3C_2 MXenes (Cl-MXene) were synthesized using an adapted Lewis acid molten salt (LAMS) method (Fig. 1a).[17] Briefly, a dried mixture of Ti_3AlC_2 powder and anhydrous zinc chloride ($ZnCl_2$) was subjected to high-temperature etching (see Fig. S1a–c for the detailed procedure). The resulting product was washed with 12 M hydrochloric acid to remove unreacted $ZnCl_2$ particles (Fig. S1d), followed by repeated rinsing with Milli-Q water until a neutral pH was achieved, yielding multilayer Cl-MXenes (Fig. 1c). The Cl-rich surface and multilayer structure of this material provide inherent resistance to water and oxygen, minimizing premature oxidation during the washing process.

To obtain single-layer flakes, the multilayer Cl-MXene was delaminated using two different approaches. Treatment with 5% (w/v) LiCl in DMSO for 24 hours produced Cl-MXene, while delamination with 5% (w/v) LiOH in DMSO for 6 hours yielded oxygen-enriched Cl-MXene (O,Cl-MXene). Both samples were subsequently washed with DMSO and *N*-methylformamide (NMF) to remove residual salts and unexfoliated material. The LiOH treatment was limited in both concentration and time to prevent excessive oxygen enrichment which may drive the oxidation of the MXene into TiO_2.

Atomic force microscopy (AFM) confirmed the successful delamination of both materials, revealing similar thicknesses for Cl-MXene (1.57 ± 0.91 nm, Fig. 1d) and O,Cl-MXene (1.55 ± 0.55 nm, Fig. 1e). The absence of TiO_2 particles on the flake surfaces and edges indicated that no significant degradation occurred during delamination. This was further supported by SEM imaging, which showed clean, single-flake structures for Cl-MXene, O,Cl-MXene, and, for comparison, *in situ* fluoride-etched $Ti_3C_2T_x$ MXene (MILD-MXene, Fig. S1h–j).

X-ray diffractometry (XRD) was used to determine the interlayer spacing (*d*-spacing) of the delaminated MXenes (Fig. 1f). The shift of the (002) peak to lower 2θ values after sintering confirmed the successful removal of the aluminum layer. Furthermore, the disappearance of the (104) peaks (Fig. S2) indicated that unreacted MAX phase particles were effectively removed through repeated washing and centrifugation. The delaminated O,Cl-MXene exhibited a larger *d*-spacing (1.26 nm) than Cl-MXene (1.11 nm), suggesting that lithium ion and NMF co-intercalation is facilitated by its oxygen-enriched surface. For reference, the even larger *d*-spacing of MILD-MXene (1.35 nm) is attributed to the co-intercalation of lithium ions and water.

Raman spectroscopy provided further evidence of surface modification (Fig. 1g). The O,Cl-MXene spectrum showed a stronger Ti–O vibrational band at $\sim$156 cm^{-1}, similar to the feature observed in MILD-MXene at $\sim$199 cm^{-1}, indicating a higher concentration of surface Ti–O bonds compared to Cl-MXene. The absence of characteristic anatase TiO_2 peaks ($\sim$410 cm^{-1}, $\sim$540 cm^{-1}, and $\sim$650 cm^{-1})[29,30] confirmed that these signals originated from the MXene surfaces and not from oxidative degradation. Peaks at $\sim$1350 cm^{-1} and $\sim$1600 cm^{-1} for both Cl-MXene and O,Cl-MXene indicated structural defects

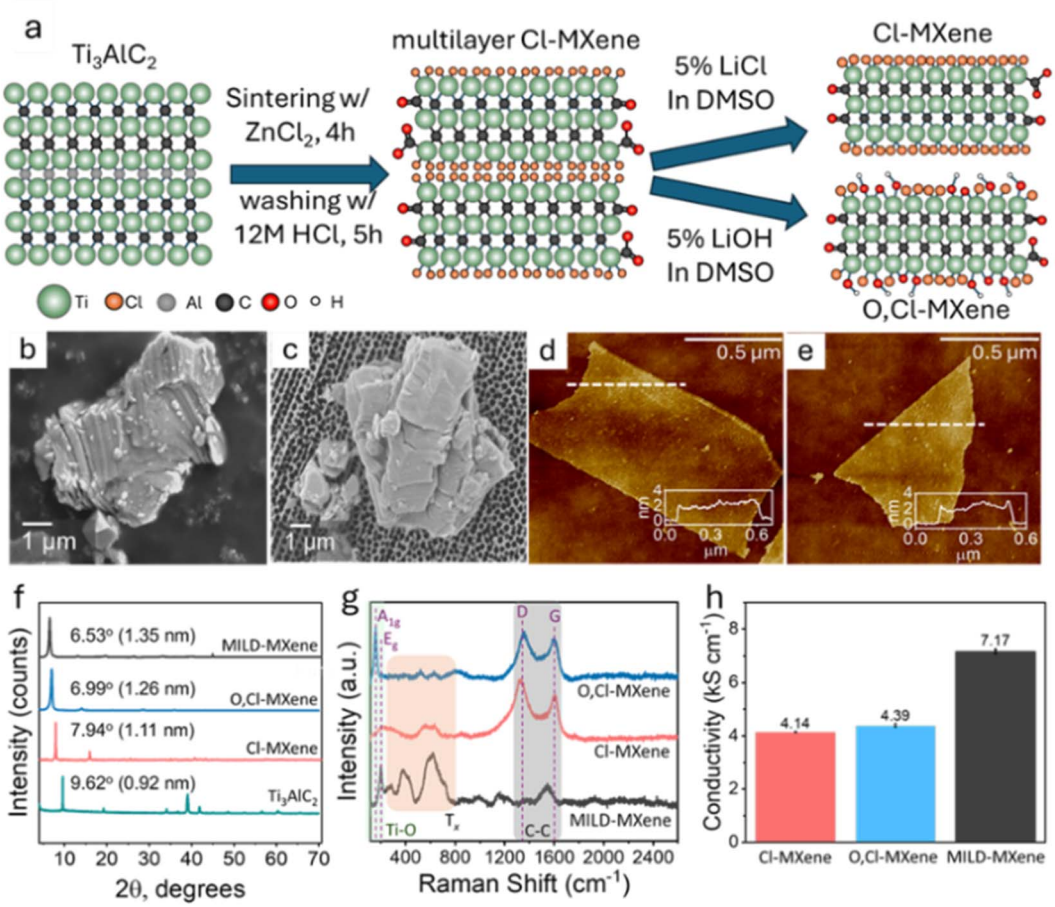

Fig. 1 (a) Illustration of the etching and delamination of the MAX phase into Cl-MXene and O,Cl-MXene. SEM images of the MAX phase (b), molten $ZnCl_2$-etched MXene after sintering and HCl washing (c), and atomic force microscopy images of delaminated (d) Cl-MXene and (e) O,Cl-MXene. (f) X-ray diffractograms of MXenes and MAX phase. (g) Raman spectra and (h) conductivity values of MXene samples.

and the presence of sp^2-hybridized carbon,[30] consistent with the harsh conditions of LAMS synthesis.[31] These defects likely contributed to the reduced electrical conductivity of both Cl-MXene (4.14 ± 0.02 kS cm^{-1}) and O,Cl-MXene (4.39 ± 0.07 kS cm^{-1}) compared to MILD-MXene (7.17 ± 0.09 kS cm^{-1}, Fig. 1h).

High-resolution X-ray photoelectron spectroscopy (XPS) provided detailed insights into the surface composition of the modified MXenes (Fig. 2 and S3). Analysis reveals a significant presence of atomic chlorine (18.42 ± 1.27 at%) and oxygen (21.21 ± 3.16 at%, Fig. S3a) in Cl-MXene, yielding an overall O/Cl ratio of 1.15 ± 0.16. However, the low Ti–O/Ti–Cl ratio (0.44 ± 0.038, Fig. S3b) indicates that Ti–Cl bonds are 2.25× more prevalent at the surface than Ti–O. On the other hand, O,Cl-MXene exhibited an increased oxygen content (27.97 ± 1.75 at%) and a higher O/Cl ratio (2.11 ± 0.10). The Ti–O/Ti–Cl ratio subsequently rose to 0.86 ± 0.08, representing a ~95% increase in oxygen-to-chlorine substitution relative to Cl-MXene. These data collectively confirm the successful surface oxygen enrichment and the partial substitution of chlorine by oxygen during the LiOH-DMSO delamination process.

Analysis of the Ti 2p spectra (Fig. 2a and S3c) revealed a site-specific mechanism, showing a pronounced decrease in Ti–Cl bonding at Ti(II) sites, compared to only a slight change at Ti(III) sites. This indicates a preferential replacement of chlorine at the less electropositive Ti(II) centers, supported by a concurrent increase in Ti–O bonds. The C 1s spectra (Fig. 2b and S3d) provided further evidence of oxidation, showing a shift towards more oxidized carbon species (increases in C–Ti–O, C–O, and C═O bonds), which suggests that the reaction also occurred at the exposed carbon atoms on the flake edges.

Direct confirmation of oxygen incorporation came from the O 1s spectra (Fig. 2c and S3e), which showed a substantial increase in C–Ti–OH and O–Ti–O bonding. The increase in C–Ti–O_x species further suggests the deprotonation of surface hydroxyls under the alkaline delamination conditions. This substitution is corroborated by the Cl 2p spectra (Fig. 2d and S3f), which showed a decrease in C–Ti–Cl bonding. This transformation is largely driven by the high nucleophilicity of oxygen and the electronegativity of chlorine, suggesting that this co-functionalization strategy is likely to be broadly applicable to any chlorine-rich MXene.

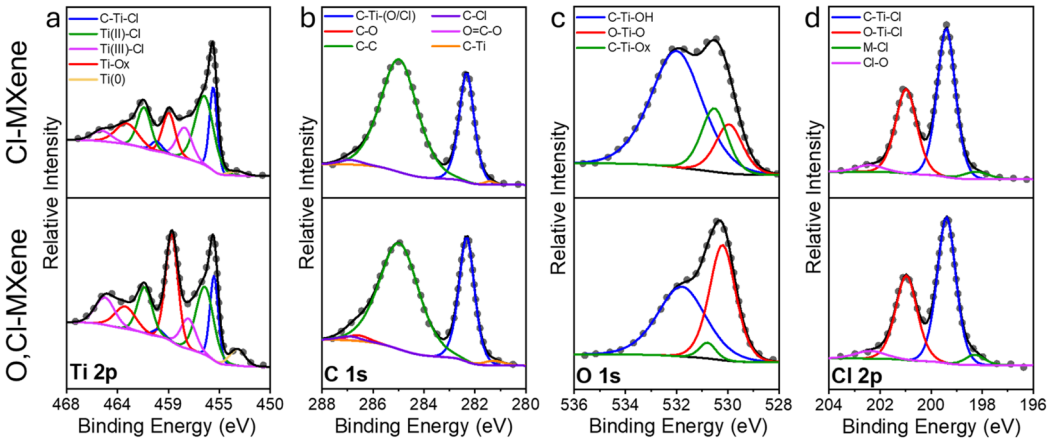

Fig. 2 Relative distribution of bond counts based on high resolution X-ray photoelectron spectra of Ti 2p (a), C 1s (b), O 1s (c), and Cl 2p (d) cores for Cl-MXene (red) and O,Cl-MXene (blue) samples.

Dispersion properties and oxidation stability

To evaluate how these surface modifications affect material properties, we investigated the dispersion stability of Cl-MXene, O,Cl-MXene, and MILD-MXene. The MXenes were transferred into a range of common solvents *via* an adapted solvent exchange procedure (Fig. S4a and b).[21,32] All dispersions were prepared at a uniform concentration of 5 mg mL^{-1} to eliminate concentration effects. Zeta potential and dynamic light scattering (DLS) measurements were then performed. Fig. 3a highlights the most representative zeta potential trends, with corresponding mobility and size data shown in Fig. 3b and c. Complete data from all seven solvents are presented in Fig. S4c–e.

In polar protic solvents, the significantly lower zeta potential of Cl-MXene (−14.5 ± 2.8 mV in water) compared to O,Cl-

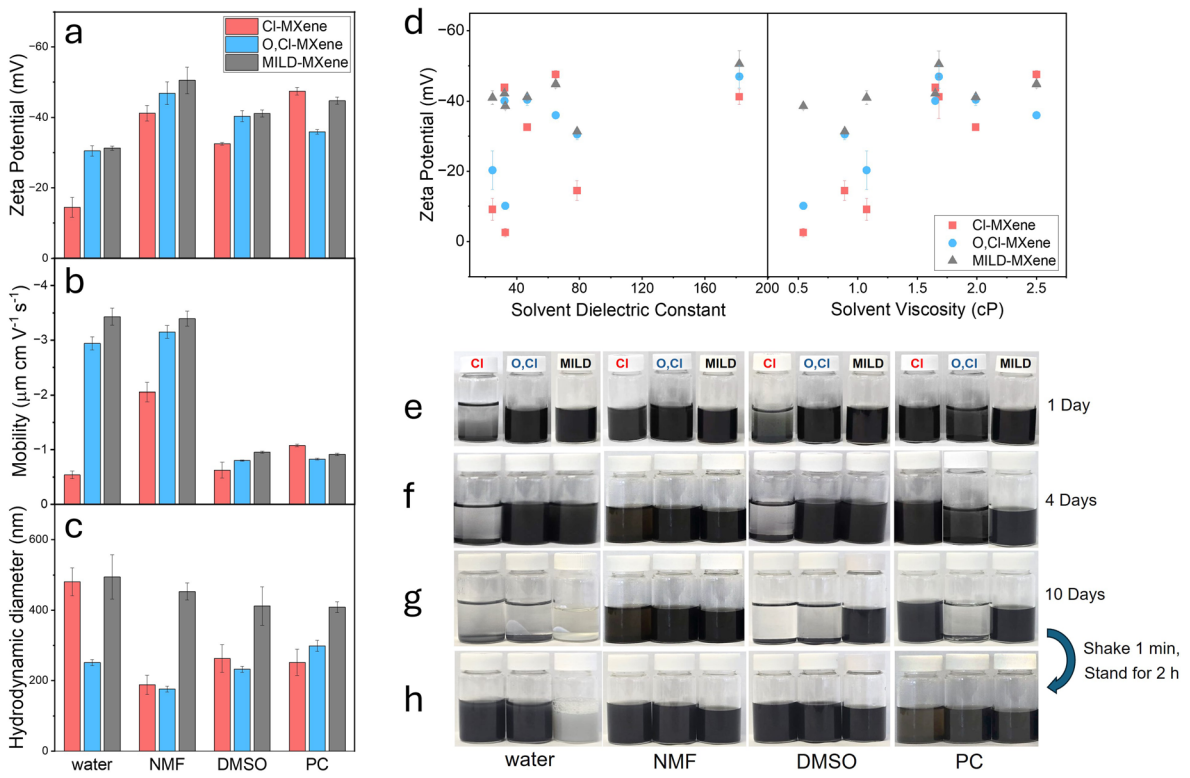

Fig. 3 Dispersion stability of MXenes in various solvents. (a) Zeta potential, (b) electrophoretic mobility, and (c) hydrodynamic diameter of Cl-MXene (red), O,Cl-MXene (blue), and MILD-MXene (gray) dispersions in water, NMF, DMSO, and PC. (d) Scatter plots of zeta potential as a function of solvent viscosity and dielectric constant. Visual stability of MXene dispersions (5 mg mL^{-1}) after standing for (e) 1 day, (f) 4 days, and (g) 10 days. (h) Digital images of dispersions after 1 minute of re-dispersion followed by 2 hours of settling.

MXene (−30.5 ± 1.5 mV) and MILD-MXene (−31.3 ± 0.6 mV) indicates a higher tendency toward flocculation, consistent with its more hydrophobic surface. This trend highlights the dispersibility advantage provided by oxygen-containing terminal groups.

A notable reversal in trend was observed in propylene carbonate (PC), where Cl-MXene exhibited a higher zeta potential (−47.5 ± 1.1 mV) than O,Cl-MXene (−36.0 ± 0.6 mV). We attribute this to the chemically heterogeneous surface of O,Cl-MXene, which may form less stable interactions with the molecular structure of PC. PC contains both hydrogen-bond acceptor sites and a large hydrophobic region, creating a mismatch with the mixed surface chemistry of O,Cl-MXene. In contrast, Cl-MXene and MILD-MXene have chemically homogeneous surfaces that facilitate more consistent solvation. These results suggest that dispersion stability is governed by specific surface–solvent interactions, although solvent viscosity may also be a contributing factor. To further understand dispersion behavior, we measured the electrophoretic mobility of each sample. Electrophoretic mobility describes the velocity of a charged particle in a fluid under an applied electric field,[33] and was calculated using the Smoluchowski equation (eqn (1)), which is suitable for polar solvent systems.

$$\mu = \frac{\varepsilon_r \varepsilon_0 \zeta}{\eta} \quad (1)$$

Here, μ is the electrophoretic mobility, ε_r is the relative permittivity of the solvent also known as its dielectric constant, ε_0 is the vacuum permittivity, η is the viscosity of the dispersion, and ζ is the zeta potential of the dispersion.

According to this relationship, mobility is directly proportional to zeta potential and inversely proportional to viscosity. While zeta potential reflects colloidal stability *via* the electric double layer, mobility describes the kinetic ease with which MXenes move through a specific solvent matrix. Our highly dilute sample concentrations (10 μg mL^{-1}) allow us to use the bulk properties of the solvent for permittivity and viscosity, making mobility a holistic parameter that incorporates both particle surface charge and solvent characteristics.

The mobility data reveal distinct trends based on solvent properties (Fig. 3b). In polar protic solvents with high dielectric constants, such as water (78.5) and NMF (182), both O,Cl-MXene and MILD-MXene exhibited higher mobility than Cl-MXene. For example, NMF's very high dielectric constant outweighed its relatively high viscosity (1.68 cP), resulting in high mobility values for all MXene samples. In contrast, mobility was significantly lower in polar aprotic solvents such as DMSO and PC, which have the highest viscosities in this study (1.99 cP and 2.50 cp, respectively) and lower dielectric constants. This trend of reduced mobility in higher viscosity solvents was also observed in other polar protic solvents (MeOH, EtOH) and in aprotic (NMP) systems (Fig. S4d). We also note that the high surface conductivity of MXenes can impede electrophoretic mobility, as has been reported for other conductive materials.[34] However, this same conductivity likely enhances colloidal stability by facilitating the formation of a stable electric double layer, which is reflected in the high zeta potentials.

These zeta potential and mobility values explain the measured hydrodynamic diameters (Fig. 3c). For instance, in water, Cl-MXene formed larger aggregates (481 ± 40 nm) than O,Cl-MXene (251 ± 9 nm), consistent with its lower zeta potential and faster aggregation. Conversely, MILD-MXene displayed the largest hydrodynamic size across most solvents. This is not attributed to aggregation, but rather to an expanded solvation shell resulting from hydrogen bonding between its oxygen-rich surface and solvent molecules, as supported by its consistently high zeta potential.

The zeta potential (ζ) of the MXenes was plotted against both the solvent viscosity (η) and dielectric constant (ε_r) to visualize how dispersion stability is influenced by these factors (Fig. 3d). Results show that for Cl-MXene, the magnitude of the zeta potential increases with higher solvent viscosity but decreases with an increasing dielectric constant. In contrast, both O,Cl-MXene and MILD-MXene exhibit an increase in ζ as η decreases and ε_r increases. This suggests that Cl-MXene dispersion stability is governed by steric interactions between the Cl-rich hydrophobic surface and the hydrophobic groups of the solvent. Conversely, both O,Cl-MXene and MILD-MXene dispersions are stabilized through strong polar interactions.

To visually evaluate dispersibility, we monitored vials containing 10 mL of each dispersion (5 m g mL^{-1}). Initial signs of aggregation were observed after one day, with Cl-MXene aggregating in water and DMSO, and O,Cl-MXene in PC (Fig. 3e). By day four, the Cl-MXene dispersions in water and DMSO had fully sedimented (Fig. 3f). In contrast, O,Cl-MXene and MILD-MXene remained well dispersed in DMSO, a stability we attribute to strong interactions between the solvent and their oxygen-containing surface groups. A similar trend was seen in PC and NMF, where oxygen-enriched MXenes showed superior stability. Overall, sedimentation was most pronounced for Cl-MXene, with four of its dispersions settling compared to only two for O,Cl-MXene (Fig. S4g). MILD-MXene showed signs of settling only in water and MeOH.

After 10 days (Fig. 3g), only Cl-MXene in NMF and PC, O,Cl-MXene in NMF, and MILD-MXene in DMSO and PC remained fully dispersed. A critical distinction emerged regarding degradation. MILD-MXene in water formed a white TiO_2 sediment, indicating severe oxidative degradation. This reveals that, despite its excellent dispersibility, MILD-MXene is highly susceptible to oxidation, as its oxygen-rich surface promotes reaction with water and atmospheric oxygen. In stark contrast, the settled Cl-MXene and O,Cl-MXene in water remained dark, demonstrating their superior resistance to degradation. This was further evidenced in NMP, a solvent prone to oxidation that turns yellowish. The absence of this colour change in Cl-MXene dispersions confirms the lack of reactive oxygen in their local environment. This suggests that for both Cl-MXene and O,Cl-MXene, the decreased hydrophilicity provided by surface chlorine groups significantly reduced MXene-water interactions. This not only hindered the rapid oxidation of MXene nanoflakes but also decreased their aqueous dispersion stability. Furthermore, the premature precipitation of the nanoflakes also limited the surface area accessible for MXene-water interactions, which further inhibited the oxidation process.

To further assess stability, we subjected 10 day-old dispersions in water, NMF, DMSO, and PC to redispersion by shaking (Fig. 3g). After standing for two hours, distinct behaviours emerged. In water, Cl-MXene and O,Cl-MXene showed only minor sedimentation, while the MILD-MXene sample had undergone near-complete conversion to white TiO_2, indicating irreversible degradation. In contrast, the dispersions in PC and DMSO readily reformed into dark, uniform dispersions, demonstrating excellent redispersibility and no signs of oxidation, which is expected in these anhydrous environments.

Collectively, our results demonstrate that O,Cl-MXene possesses the broad dispersibility of oxygen-rich MXenes combined with the oxidation resistance of its chlorine-terminated counterpart. Enrichment with oxygen groups increases surface polarity, thereby enhancing dispersibility in a wider range of solvents than Cl-MXene. Simultaneously, the retained chlorine groups impart a protective, water-resistant characteristic, yielding far greater oxidation resistance than MILD-MXene. This strategic co-functionalization produces materials with uniquely balanced properties that may have implications for electrochemical behavior.

Electrochemical behaviour

The electrochemical performance of MXenes is governed by the interaction between their surface chemistry and the electrolyte, which critically determines ion accessibility to the interlayer space. This leads to either inhibited or promoted electrochemical activity. To examine this, we performed cyclic voltammetry (CV) using drop-cast MXene films on glassy carbon working electrodes in both organic and aqueous media. Fig. 4a shows CVs in a propylene carbonate (PC) electrolyte with lithium bis(trifluoromethanesulfonyl)imide (LiTFSi) salt, while Fig. 4b and c present data from aqueous electrolyte solutions.

Our results reveal that the electrochemical performance of these MXenes is fundamentally governed by their surface chemistry. The lower capacitance of Cl-MXene indicates that the electronegative surface chlorine atoms limit both the MXene-solvent and MXene-cation interactions. These observations are consistent with previous findings on the electrochemical performance of chlorine terminated MXenes across different electrolyte systems, which reported capacitance values of 1–5 F g^{-1} at current densities of 10–100 A g^{-1} in various aqueous electrolytes.[35–37] The increased presence of surface oxygen groups facilitates stronger MXene-ion interactions, enhancing both capacitive and pseudocapacitive processes. In contrast, the oxygen-functionalized surfaces of O,Cl-MXene and MILD-MXene facilitate stronger cation interactions, creating a favourable environment for capacitive processes. As shown in Fig. 4d, O,Cl-MXene consistently achieves significantly higher capacitance than Cl-MXene. This performance gap is particularly notable in the LiTFSi/PC system, where the capacitance for O,Cl-MXene (61.9 ± 6.4 F g^{-1}) is ~10 times greater than that of Cl-MXene (7.3 ± 1.6 F g^{-1}). Similar tenfold and 4.5-fold improvements were observed in aqueous LiCl and KCl electrolytes, respectively.

We attribute this enhanced performance to two factors. First, the abundant oxygen groups on O,Cl-MXene strongly interact with both solvent molecules and ions, promoting better electrolyte penetration, as corroborated by the high performance of MILD-MXene. Second, the larger *d*-spacing of O,Cl-MXene (1.26 nm) compared to Cl-MXene (1.11 nm) provides a more accessible surface area for charge storage. The combined effect of these factors is directly evidenced by the larger integrated areas of the O,Cl-MXene CV curves.

We further investigated the influence of surface composition on electrochemical stability by determining the stable operating potential window for each sample (Fig. 4e). The window was obtained by scanning at 10 mV s^{-1} from the open circuit potential (OCV) towards the negative and positive potentials, gradually increasing the range until the electrode exhibited failure. Then, the sample electrode is scanned from the maximum negative to the maximum positive potentials at increasing rates to confirm stability within the determined window (Fig. S5). Both Cl-MXene and O,Cl-MXene exhibited wider stable potential windows that extend to positive potentials across all electrolytes, indicating superior resistance to anodic oxidation. This suggests that surface chlorine atoms effectively inhibit titanium oxidation, stabilizing the MXene structure at more positive potentials. Chlorine chemistry is a known inhibiting factor in electrolytic oxygen-evolution reactions (OER)[38] due to its lower oxidation potential compared to oxygen in neutral pH. Further utilization of this property may enable surface processes that require large positive potentials[39] while minimizing the risk of MXene degradation. The wider anodic stability combined with weak interactions with ionic species can also be utilized to design water-splitting electrolytic energy harvesting strategies using seawater without the risk of producing harmful gases like Cl_2.[40] However, both the Cl-MXene and O,Cl-MXene showed narrower cathodic windows compared with MILD-MXenes across all systems, suggesting less surface stability at more negative potentials. This is due to the highly electronegative surface Cl atoms, which can act as effective hydrogen adsorbents while being less reactive than surface oxygen species, which are key desirable properties for catalytic hydrogen evolution reactions (HER).[41] However, this reaction may also cause extensive reduction of the surface Ti atoms, which may trigger the release of chloride terminations and expose the surface to water attack. These findings demonstrate the impact of variations in surface composition and chemistry on both the capacitive performance and operating voltage stability of MXenes.

We also studied the ion kinetics at these different MXene surfaces across various electrolytes using electrochemical impedance spectroscopy (EIS). This technique allows examination of processes across different frequency regions, each representative of different electrochemical phenomena.[42] The Nyquist plots were fitted in a Randles–Ershler circuit model[43] to include a diffusion control parameter *a*, which accounts for the influence ion diffusion across the bulk media during the capacitive processes. The calculated circuit parameters from the obtained EIS data are shown in Fig. S6. In the LiTFSi in PC system (Fig. 4f), both the Cl-MXene and O,Cl-MXene samples show much higher equivalent series resistance (ESR, 120–150 Ω) at high frequency compared to MILD-MXene (~30 Ω). PC has

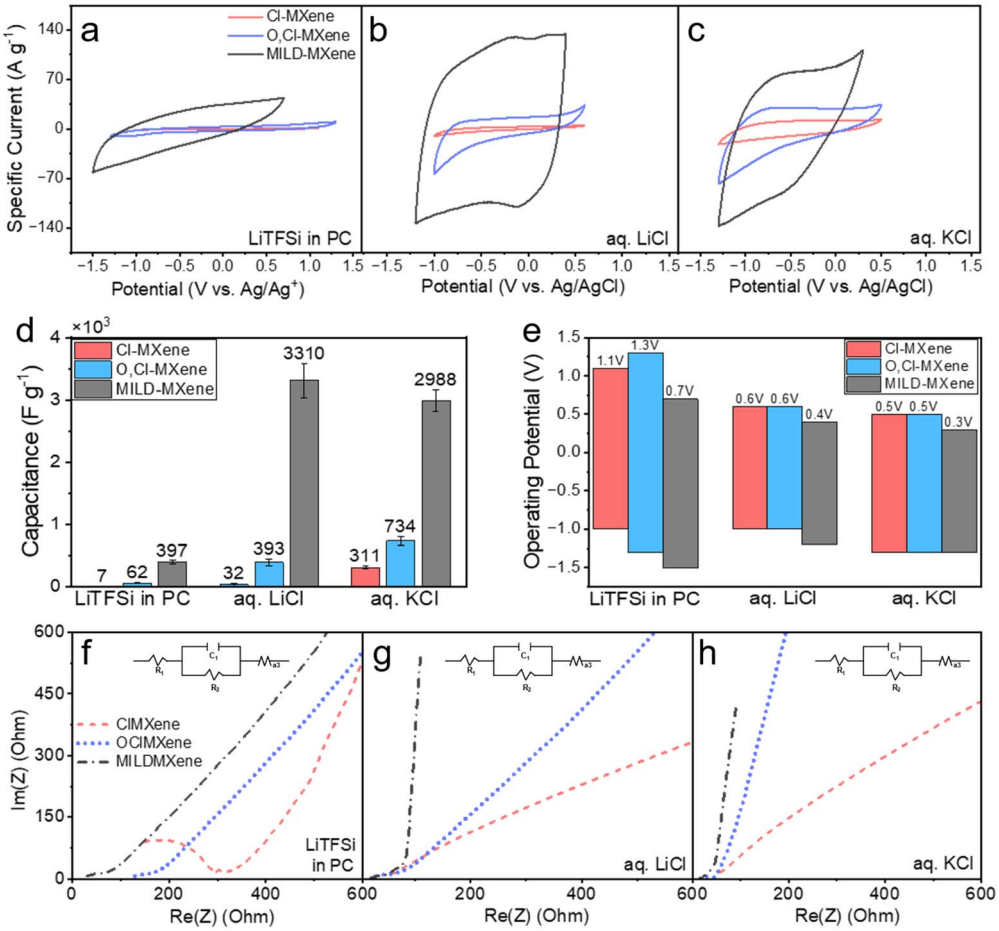

Fig. 4 Cyclic voltammograms of Cl-MXene (red), O,Cl-MXene (blue), and MILD-MXene (gray) in (a) LiTFSi in PC, (b) aqueous LiCl, and (c) aqueous KCl. (d) Comparison of capacitance values and (e) stable operating voltage windows of the MXene samples. Nyquist plots and superimposed Randles–Ershler circuit models for Cl-MXene (red, dashed), O,Cl-MXene (blue, dotted), and MILD-MXene (black, dash-dots) from electrochemical impedance spectroscopy in (f) LiTFSi in PC, (g) aqueous LiCl, and (h) aqueous KCl.

a relatively high viscosity at room temperature (2.3–2.7 cP) which impedes with the Li^+ mobility, which reflects on the ESR. Also, the significant presence of chlorine terminations decreased the affinity of both Cl-MXene and O,Cl-MXene with Li^+, which explains the higher ESR compared to MILD-MXene. The plots also show clear diffusion-controlled kinetics for all samples, as suggested by the characteristic ~45° Warburg impedance lines extending into the low-frequency region. However, increased presence of both chlorine and oxygen terminations at the O,Cl-MXene surface enhances affinity to both PC and Li^+, lowering its ESR (~120 Ω) compared to Cl-MXene. The same effect also impacts Cl-MXene, as its electronegative Cl-rich surface severely limits interactions with Li^+. MILD-MXene showed the slowest kinetics among the three samples, possibly because oxygen and hydroxyl terminations and trapped interlayer water hinder PC intercalation.

In aqueous LiCl (Fig. 4g) electrolyte, ESR is greatly reduced due to the high mobility of Li^+ in aqueous solution. In contrast to the organic electrolyte, MILD-MXene consistently shows the lowest ESR and fastest kinetics, followed by O,Cl-MXene, while Cl-MXene exhibits the slowest and most diffusion-controlled kinetics, which is expected due to the hydrophobic Cl-terminations. O,Cl-MXene trends in the middle of both Cl-MXene and MILD-MXene due to the mixed chlorine and oxygen groups at its surface.

In aqueous KCl (Fig. 4h) electrolyte, all three samples show improved kinetics, likely due to the higher mobility and smaller hydrated radius of K^+ ions, which can easily intercalate into MXene interlayer spaces. These results illustrate that the MILD method typically produces MXenes with larger, more open interlayer spacing, which show improved electrochemical kinetic in aqueous electrolyte, while O,Cl-MXene perform better in polar organic solvents like PC because of the mixed chlorine and oxygen groups at its surface. Overall, this work demonstrates the influence of contrasting surface chemical properties of both Cl and O on capacitive processes, which could be employed to control surface ion kinetics in different electrolyte systems with MXene.

Conclusions

This study introduces a delamination strategy to synthesize oxygen-enriched, chlorine-terminated MXenes (O,Cl-MXene) by treating LAMS-synthesized Cl-MXene with LiOH in DMSO.

Comprehensive characterization confirmed successful surface modification, revealing a ~150% increase in Ti–O species at the surface through oxygen addition and the substitution of labile –Cl terminal atoms. These tailored changes directly enhanced the material's properties. The introduced oxygen groups improved electric double layer formation, yielding zeta potential values comparable to conventional MILD-MXene and enabling superior dispersibility across various solvents. Furthermore, O,Cl-MXene exhibited excellent redispersibility and superior oxidation resistance, outperforming both counterparts. Electrochemically, this mixed-termination strategy proved highly effective. O,Cl-MXene achieved 5× to 10× greater capacitance than Cl-MXene across various electrolytes. The oxidation-resistant surface also resulted in enhanced anodic potential stability (+~0.2 V) compared to oxygen-rich MILD-MXenes. Furthermore, we showed that the incorporation of oxygen generally enhances ion kinetics at the MXene surface. Ultimately, we demonstrate that mixed chlorine/oxygen terminations simultaneously enhance MXene stability and performance without hazardous fluoride-based etching, paving the way for safer, high-performance, and stable MXene-based applications.

Experimental

Synthesis of chlorine-terminated MXene (Cl-MXene)

Two grams of pre-dried Ti_3AlC_2 MAX phase (Carbon-Ukraine Ltd, particle size <40 μm, vacuum-dried at 105 °C for 12 hours) were thoroughly mixed with 18 grams of anhydrous zinc chloride ($ZnCl_2$, 99%, Sigma-Aldrich) in a 50 mL N_2-aerated centrifuge tube for 5 minutes. The mixture was transferred to a rectangular alumina crucible, covered with graphite foil, and sintered in a tube furnace (Carbolite STF16/610) under a Lewis acid molten salt protocol. The temperature program was as follows: heat at 5 °C min^{-1} to 250 °C and hold for 3 hours; then heat at 5 °C min^{-1} to 400 °C and hold for 3 hours; and finally, heat at 5 °C min^{-1} to 640 °C and hold for 4 hours before cooling to room temperature at 5 °C min^{-1}.

The sintered product was transferred to a vacuum filtration setup with cellulose filter paper. Excess $ZnCl_2$ was dissolved by adding 300 mL of deionized water. The solids were then transferred to a 150 mL beaker, treated with 50 mL of 12 M hydrochloric acid (HCl, Sigma-Aldrich) under stirring for 5 hours to remove byproducts. The solids were subsequently transferred to a 200 mL HDPE bottle with 100 mL of water. The mixture was centrifuged (2000 rpm, 716 rcf, 30 min), and the supernatant was discarded. The residue was washed four times with 100 mL of deionized water to remove residual HCl and neutralize the pH. The multilayer Cl-MXene was dried under vacuum at room temperature.

Synthesis of MILD-MXene

For comparison, $Ti_3C_2T_x$ MXene was synthesized *via* the minimally intensive layer delamination (MILD) method. A solution of 1.6 g lithium fluoride (99%, Sigma-Aldrich) in 20 mL of 9 M hydrochloric acid (37%, Sigma-Aldrich) was prepared and stirred for 5 minutes. Then, 1 g of Ti_3AlC_2 MAX phase powder (Carbon-Ukraine Ltd, particle size <40 μm) was added and stirred for 28 hours at room temperature. The mixture was diluted with deionized water and centrifuged (3000 rpm, 1532 rcf, 5 minutes) to remove acid. This washing cycle was repeated until the pH reached ~6.0.

To remove unreacted MAX phase, the dispersion was centrifuged (1500 rpm, 383 rcf, 30 min), and the dark green supernatant containing delaminated MXene was collected. The MXene was concentrated by centrifugation (7000 rpm, 8341 rcf, 30 minutes), and the precipitate was vacuum-dried to determine the concentration.

Delamination of Cl-MXene

Multilayer Cl-MXenes were delaminated in 30 mL of 5% (w/v) lithium chloride (LiCl, 99%, Sigma-Aldrich) in dimethyl sulfoxide (DMSO, Sigma-Aldrich) by shaking at 70 rpm for 24 hours on a 90-degree rotator (Thermo Fisher Scientific). The mixture was centrifuged (8500 rpm, 12 298 rcf, 30 minutes), and the residue was washed once with DMSO to remove excess LiCl, followed by centrifugation (8500 rpm, 12 298 rcf, 30 minutes) to obtain delaminated Cl-MXene.

For the oxygen-enriched Cl-MXene (O,Cl-MXene) synthesis, the same procedure was repeated using 5% (w/v) lithium hydroxide (LiOH, 99%, Sigma-Aldrich) in DMSO for 6 hours. The product was washed with DMSO and centrifuged (8500 rpm, 12 298 rcf, 30 minutes) to obtain delaminated O,Cl-MXene.

Dispersion of Cl-MXene, O,Cl-MXene, and MILD-MXene

Delaminated dispersions were centrifuged (8500 rpm, 12 298 rcf, 30 minutes), and the residue was mixed with the desired solvent, shaken for 10 minutes, and centrifuged again (8500 rpm, 12 298 rcf, 30 minutes). This washing step was repeated twice before final dispersion in the same solvent. The process was done carefully to prevent premature degradation due to mechanical damage.[44] A 10 mL dispersion (5 mg mL^{-1}) was prepared in a 20 mL vial and stored undisturbed for 48 hours. The solvents used were ultrapure water (18.2 MΩ at 25 °C), methanol (99%, Sigma-Aldrich), ethanol (95%, Sigma-Aldrich), *N*-methylformamide (99%, Sigma-Aldrich), dimethyl sulfoxide (99%, Sigma-Aldrich), propylene carbonate (99%, Sigma-Aldrich), and *N*-methyl-2-pyrrolidone (99%, Sigma-Aldrich). All solvents were used as received without further purification.

Characterization

Images of MAX phase and MXene flakes were acquired using a Zeiss Gemini 460 scanning electron microscope (Zeiss, Germany) operating at 5 kV accelerating voltage, 80 pA probe current, and 5 mm working distance in SE2 mode.

Flake thickness was measured with a Bruker DimensionEdge atomic force microscope (AFM, Bruker, USA) at a scan rate of 0.6 Hz. Samples were prepared by drop-casting MXene dispersions (1 μg mL^{-1}) onto activated silicon wafers (pre-cleaned

with H_2SO_4 (18 M) and H_2O_2 (30 vol% at a 5 : 1 volume ratio) for 12 hours) and vacuum drying for 6 hours.

X-ray diffraction patterns were recorded on a PANalytical X'Pert Powder diffractometer (UK) using Cu Kα radiation (λ = 1.54 Å), a 2θ step size of 0.013°, and a dwell time of 100 milliseconds. Samples were prepared by drop-casting MXene dispersions (1 mg mL^{-1}) onto zero-diffraction silicon wafers and vacuum-drying for 6 hours.

Raman spectra were acquired using a Renishaw Raman Microscope (Renishaw, UK) with a 514 nm Ar^+ laser at 5% power. MXene dispersions (1 mg mL^{-1}) were drop-cast onto aluminum substrates and vacuum-dried for 6 hours prior to analysis.

Hydrodynamic size and zeta potential were measured using a Nano ZS Zetasizer (Malvern Instruments, UK). For size measurements, 1 mL of aqueous dispersion (10 μg mL^{-1}) was placed in a disposable sizing cuvette. For zeta potential measurements in aqueous dispersions, 1 mL (10 μg mL^{-1}) was loaded into a folded capillary cell. For non-aqueous solvents, a dip cell (ZEN1002) was used with a clear glass cuvette. The electrode was pre-rinsed with pure solvent. Each sample underwent five trials with 20 measurements per trial (100 data points in total).

High resolution X-ray photoelectron spectroscopy (XPS) was performed using a K-Alpha+ system (Thermo Fisher Scientific, USA) under ultra-high vacuum (5×10^{-8} mbar). Films were secured with conductive carbon tape. Survey scans (0 to 1350 eV) were conducted using a pass energy of 200 eV and 1 eV resolution. High-resolution core spectra were acquired at pass energy of 50 eV and step size of 0.1 eV over the following ranges: 452 to 468 eV for Ti 2p, 526 to 537 eV for O 1s, and 195 to 205 eV for Cl 2p. Five locations per sample were analyzed with 10 scans each. Data processing was performed using CasaXPS (Casa Software Ltd, UK) and Avantage (Thermo Fisher Scientific, USA) for background correction, normalization, deconvolution, peak fitting, and compositional analysis.

Electrochemical studies were performed using a SP 300 potentiostat (Biologic, France) with a three-electrode setup. For the aqueous LiCl and KCl systems, Ag/AgCl in saturated KCl reference and porous graphite counter electrodes were used. For the non-aqueous LiTFSi/PC system, pure Ag wire pseudo-reference and porous graphite counter electrodes were used. The working electrode was prepared by drop-casting 10 μg of MXene dispersion onto a polished glassy carbon electrode, air-dried, and coated with 5 μL of 5% Nafion to ensure adhesion. Electrochemical impedance spectroscopy (EIS) was performed within the range of 200 kHz to 100 mHz, at an amplitude of 10 mV. The electrodes were precycled 5 times at 10 mV s^{-1} prior to the analysis to ensure stability.

Author contributions

K. P. M. carried out the experiments and drafted the manuscript. L. C. H., J. Z., K. A. S. M., and J. M. R. helped with the conceptualisation, as well as determination of the research aim and targets. X. L., M. A. J, R. M.C. R. R., E. S. A., and B. H. helped with sample preparation, characterisation, and data processing.

Conflicts of interest

There are no conflicts to declare.

Data availability

The data supporting this article have been included as part of the supplementary information (SI). Supplementary information is available. See DOI: https://doi.org/10.1039/d6ta00904b.

Acknowledgements

The authors acknowledge the Australian Research Council (IH210100023), the Australian National Fabrication Facility (Victorian node at Deakin University), the Melbourne Center for Nanofabrication, the Deakin-CSIRO InSitX X-ray facility, the Deakin's Analytical Instrumentation and Advanced Characterization facilities. J.M.R. acknowledges support from The Hong Kong Polytechnic University under the Strategic Hiring Scheme. J.Z. and K.A.S.U. acknowledge funding support from their respective Deakin University Postdoctoral Research Fellowships (DUPRF).

References

1 M. Naguib, M. Kurtoglu, V. Presser, J. Lu, J. Niu, M. Heon, L. Hultman, Y. Gogotsi and W. Barsoum Michel, *Adv. Mater.*, 2011, **23**, 4248–4253.
2 M. Ghidiu, M. R. Lukatskaya, M.-Q. Zhao, Y. Gogotsi and M. W. Barsoum, *Nature*, 2014, **516**, 78–81.
3 K. Chatterjee, J. Tabor and T. K. Ghosh, *Fibers*, 2019, **7**, 51.
4 S. Zhu, M. Wang, Z. Qiang, J. Song, Y. Wang, Y. Fan, Z. You, Y. Liao, M. Zhu and C. Ye, *Chem. Eng. J.*, 2021, **406**, 127140.
5 J. Zhang, N. Kong, S. Uzun, A. Levitt, S. Seyedin, P. A. Lynch, S. Qin, M. Han, W. Yang, J. Liu, X. Wang, Y. Gogotsi and J. M. Razal, *Adv. Mater.*, 2020, **32**, 2001093.
6 X. Zhu, B. Liu, H. Hou, Z. Huang, K. M. Zeinu, L. Huang, X. Yuan, D. Guo, J. Hu and J. Yang, *Electrochim. Acta*, 2017, **248**, 46–57.
7 M. Naguib, J. Come, B. Dyatkin, V. Presser, P.-L. Taberna, P. Simon, M. W. Barsoum and Y. Gogotsi, *Electrochem. Commun.*, 2012, **16**, 61–64.
8 Y. Dall'Agnese, M. R. Lukatskaya, K. M. Cook, P.-L. Taberna, Y. Gogotsi and P. Simon, *Electrochem. Commun.*, 2014, **48**, 118–122.
9 K. A. S. Usman, Y. Yao, C. J. O. Bacal, J. Zhang, K. L. Jarvis, P. A. Lynch, P. Mota-Santiago, S. Qin, M. Naebe, L. C. Henderson, D. Y. Hegh, B. J. Allardyce and J. M. Razal, *Adv. Mater. Interfaces*, 2023, **10**, 2201634.
10 S. Seyedin, J. Zhang, K. A. S. Usman, S. Qin, A. M. Glushenkov, E. R. S. Yanza, R. T. Jones and J. M. Razal, *Glob. Chall.*, 2019, **3**, 1900037.
11 Y.-Z. Zhang, K. H. Lee, D. H. Anjum, R. Sougrat, Q. Jiang, H. Kim and H. N. Alshareef, *Sci. Adv.*, 2018, **4**, eaat0098.
12 H. Liao, X. L. Guo, P. B. Wan and G. H. Yu, *Adv. Funct. Mater.*, 2019, **29**, 1904507.
13 M. Naguib and Y. Gogotsi, *Acc. Chem. Res.*, 2015, **48**, 128–135.

14 C. Wang, H. Shou, S. Chen, S. Wei, Y. Lin, P. Zhang, Z. Liu, K. Zhu, X. Guo, X. Wu, P. M. Ajayan and L. Song, *Adv. Mater.*, 2021, **33**, 2101015.
15 J. Chen, M. Chen, W. Zhou, X. Xu, B. Liu, W. Zhang and C. Wong, *ACS Nano*, 2022, **16**, 2461–2470.
16 L.-Y. Xiu, Z.-Y. Wang and J.-S. Qiu, *Rare Met*, 2020, **39**, 1237–1238.
17 T. Zhang, K. Shevchuk, R. J. Wang, H. Kim, J. Hourani and Y. Gogotsi, *Chem. Mater.*, 2024, **36**, 1998–2006.
18 M. Li, J. Lu, K. Luo, Y. Li, K. Chang, K. Chen, J. Zhou, J. Rosen, L. Hultman, P. Eklund, P. O. Å. Persson, S. Du, Z. Chai, Z. Huang and Q. Huang, *J. Am. Chem. Soc.*, 2019, **141**, 4730–4737.
19 Y. Liu, Q. Jia, Y. Yan, N. Yuan, W. Luo, X. Yuan, L. Wang and S. Guo, *Ceram. Int.*, 2024, **50**, 8546–8550.
20 D. Wang, C. Zhou, A. S. Filatov, W. Cho, F. Lagunas, M. Wang, S. Vaikuntanathan, C. Liu, R. F. Klie and D. V. Talapin, *Science*, 2023, **379**, 1242–1247.
21 K. P. Marquez, M. A. Judicpa, R. A. J. Malenab, R. M. C. R. Ramos, E. Austria, Jr., B. Akhavan, L. C. Henderson, K. A. S. Usman, J. Zhang and J. M. Razal, *ACS Appl. Mater. Interfaces*, 2025, **17**, 15877–15885.
22 S. Huang and V. N. Mochalin, *Inorg. Chem.*, 2019, **58**, 1958–1966.
23 S. Gong, F. Zhao, H. Xu, M. Li, J. Qi, H. Wang, Z. Wang, X. Fan, C. Li and J. Liu, *J. Colloid Interface Sci.*, 2022, **615**, 643–649.
24 M. Jiang, D. Wang, Y.-H. Kim, C. Duan, D. V. Talapin and C. Zhou, *Angew. Chem.*, 2024, **136**, e202409480.
25 V. Kamysbayev, A. S. Filatov, H. Hu, X. Rui, F. Lagunas, D. Wang, R. F. Klie and D. V. Talapin, *Science*, 2020, **369**, 979–983.
26 D. D. Kruger, H. García and A. Primo, *Adv. Sci.*, 2024, **11**, 2307106.
27 J. Choi, M. S. Oh, A. Cho, J. Ryu, Y.-J. Kim, H. Kang, S.-Y. Cho, S. G. Im, S. J. Kim and H.-T. Jung, *ACS Nano*, 2023, **17**, 10898–10905.
28 M. Öper, U. Yorulmaz, C. Sevik, F. Ay and N. Kosku Perkgöz, *J. Appl. Phys.*, 2022, **131**, 025304.
29 H. C. Choi, Y. M. Jung and S. B. Kim, *Vib. Spectroscop.*, 2005, **37**, 33–38.
30 S. Adomaviciute-Grabusove, A. Popov, S. Ramanavicius, V. Sablinskas, K. Shevchuk, O. Gogotsi, I. Baginskiy, Y. Gogotsi and A. Ramanavicius, *ACS Nano*, 2024, **18**, 13184–13195.
31 T. Azam, M. S. Khalid and Z.-S. Wu, *Mater. Today*, 2025, **82**, 289–320.
32 S. Seyedin, J. Zhang, K. A. S. Usman, S. Qin, A. M. Glushenkov, E. R. S. Yanza, R. T. Jones and J. M. Razal, *Glob. Chall.*, 2019, **3**, 1900037.
33 J. F. Miller, K. Schätzel and B. Vincent, *J. Colloid Interface Sci.*, 1991, **143**, 532–554.
34 P. Leroy, C. Tournassat, O. Bernard, N. Devau and M. Azaroual, *J. Colloid Interface Sci.*, 2015, **451**, 21–39.
35 M. Y. Jung, J. Park, S. Pandey, S. Eom, J.-W. Son, Y. J. Yun and Y. Jun, *J. Energy Storage*, 2025, **135**, 118283.
36 K. Kawai, M. Fujita, R. Iizuka, A. Yamada and M. Okubo, *2D Mater.*, 2023, **10**, 014012.
37 L. Zhu, J. Ji, H. Yin and H. Zhao, *Energy Fuels*, 2023, **37**, 5607–5612.
38 J. Guo, Y. Zheng, Z. Hu, C. Zheng, J. Mao, K. Du, M. Jaroniec, S.-Z. Qiao and T. Ling, *Nat. Energy*, 2023, **8**, 264–272.
39 N. Shpigel, A. Chakraborty, F. Malchik, G. Bergman, A. Nimkar, B. Gavriel, M. Turgeman, C. N. Hong, M. R. Lukatskaya, M. D. Levi, Y. Gogotsi, D. T. Major and D. Aurbach, *J. Am. Chem. Soc.*, 2021, **143**, 12552–12559.
40 G. Bahuguna and F. Patolsky, *ACS Mater. Lett.*, 2024, **6**, 3202–3217.
41 A. Kumari, S. Singh, R. Munde, A. U. Bashir, P. P. Ingole and D. Ghosh, *J. Mater. Chem. A*, 2025, (13), 42410–42426.
42 A. C. Lazanas and M. I. Prodromidis, *ACS Meas. Sci. Au*, 2023, **3**, 162–193.
43 S. Dhillon and R. Kant, *J. Chem. Sci.*, 2017, **129**, 1277–1292.
44 K. A. S. Usman, R. P. Ibabao, K. M. D. Sisican, M. Judicpa, R. M. C. R. Ramos, K. P. Marquez, J. Zhang, E. S. Austria, B. Akhavan, A. Thakur, N. Chandran B. S, L. C. Henderson, B. Anasori and J. M. Razal, *J. Mater. Chem. A*, 2026, **14**, 7541–7551.

